

# Compaction and dilation rate dependence of stresses in gas-fluidized beds

Sung Joon Moon, I. G. Kevrekidis, and S. Sundaresan

Department of Chemical Engineering & Program in Applied and Computational Mathematics  
Princeton University, Princeton, NJ 08544

A particle dynamics-based hybrid model, consisting of monodisperse spherical solid particles and volume-averaged gas hydrodynamics, is used to study traveling planar waves (one-dimensional traveling waves) of voids formed in gas-fluidized beds of narrow cross-sectional areas. Through ensemble-averaging in a co-traveling frame, we compute solid phase continuum variables (local volume fraction, average velocity, stress tensor, and granular temperature) across the waves, and examine the relations among them. We probe the consistency between such computationally obtained relations and constitutive models in the kinetic theory for granular materials which are widely used in the two-fluid modeling approach to fluidized beds. We demonstrate that solid phase continuum variables exhibit appreciable "path dependence", which is not captured by the commonly used kinetic theory-based models. We show that this path dependence is associated with the large rates of dilation and compaction that occur in the wave. We also examine the relations among solid phase continuum variables in beds of cohesive particles, which yield the same path dependence. Our results both for beds of cohesive and non-cohesive particles suggest that path-dependent constitutive models need to be developed.

PACS numbers:

## I. INTRODUCTION

Flows involving gas-particle mixtures are ubiquitous in nature and in engineering practice [1, 2, 3, 4]. Homogeneous flows are often unstable, and spatiotemporal structures such as traveling waves, clusters and streamers of particles, and bubble-like voids are commonly observed in fluidized beds. The origin of the instabilities leading to these structures has been studied extensively in the literature [2, 3, 4, 5, 6].

The number of particles present in these flows is large, rendering detailed description of the motion of all the particles impractical. Hence, macroscopic flow characteristics are often probed through analysis of continuum models derived by averaging the equations governing the motion of the individual particles and the interstitial fluid. In this approach, the fluid and solid phases are treated as interpenetrating continua, and locally-averaged quantities such as the volume fractions and velocities of fluid and solid phases appear as dependent variables. The details of flow at the level of individual particles appear in the averaged equations through the effective fluid and particle phase stresses and the inter-phase interaction force, for which one must postulate constitutive models. It is now known that inhomogeneous structures such as traveling waves and bubble-like voids in fluidized beds can be reproduced in a qualitatively correct manner through very simple constitutive models for the above-mentioned quantities (see e.g., Glasser et al. [7]). Quantitative predictions are still elusive in many cases.

The derivation of constitutive models for these terms has been studied extensively in the literature. For example, the kinetic theory of granular materials (KTGM) for the quantification of the stresses in a rapidly shearing assembly of particles undergoing only binary collisions has been discussed by many authors [3, 4, 8, 9, 10, 11, 12], and it has found widespread applications in many gas-particle flow problems [4, 13]. Many of the early studies of the kinetic theory focused on spherical, uniformly sized, non-cohesive particles, while more recently there have been attempts to extend it to slightly cohesive systems (see e.g., Kim and Arastoopour [14]). Particle dynamics simulations of shear flow of nearly homogeneous assemblies of non-cohesive particles have been used to validate the kinetic theory [12, 15, 16, 17].

As mentioned above, gas-particle flows in fluidized beds readily form inhomogeneous structures, where the particle assembly undergoes compaction and dilation in an alternating periodic manner while also undergoing a shear. For example, in fluidized beds, this results from the flow patterns created by a succession of bubble-like voids rising through the bed. Quite frequently, such effects occur over length scales in the range of 10–50 particle diameters [6, 13], and the effect of the rate of compaction or dilation accompanying inhomogeneous flows at such length scales on the rheological characteristics is largely unknown.

While the KTGM does include a bulk viscosity term to account for the effect of compaction/dilation rate on the solid phase pressure, the adequacy of this correction remains untested. A good understanding of the typical rates of compaction and dilation that can occur in fluidized gas-particle suspensions and their influence on the stresses is a necessary step in the quest for constitutive models that can lead to quantitative predictions of their flow behavior. The first goal of this study is to ana-

---

Corresponding author: sundar@princeton.edu; 609-258-4583 (tel); 609-258-0211 (fax).

lyze a simple, idealized gas-particle flow problem where a particle assembly undergoes compaction and dilation in an alternating manner and also manifests spatial inhomogeneity that is typical of fluidized suspensions, and probe how the stresses are influenced by compaction or dilation events. To this end, we have carried out particle dynamics-based hybrid simulations of a periodic assembly of uniformly sized, spherical, non-cohesive, frictional and inelastic particles fluidized by a gas, and created an inhomogeneous flow pattern that takes the form of a one-dimensional (vertically) traveling wave (1D-TW). In this approach, solid phase stresses are determined through particle-particle interactions, rather than by postulated constitutive models, and various inter-particle forces such as cohesive forces can readily be accounted for without introducing additional assumptions. By traveling along this wave and averaging over many realizations, we have extracted the spatial variation of various ensemble-averaged quantities. It will be shown that the stresses manifest strong path dependence. When the assembly undergoes dilation, the stress levels are very small and are essentially independent of the rate of dilation; in contrast, when compaction occurs, the stresses depend strongly on the rate of compaction.

We have also extended these simulations to include inter-particle attractive forces; specifically, we considered a simple model to capture van der Waals force between the particles. It will be shown through an analysis of traveling waves in modestly cohesive systems that the path dependence is even greater in cohesive systems.

The rest of the paper is organized as follows. The model we use, a particle dynamics model coupled with volume-averaged gas hydrodynamics, is described in Sec. II. The traveling wave structures and properties obtained in our simulations of beds of non-cohesive particles are presented in Sec. IIIA. In Sec. IIIB, solid phase continuum variables across the waves are analyzed and assumptions used in KTGM are probed. The waves formed in beds of moderately cohesive particles are analyzed in Sec. IIIC, followed by conclusions in Sec. IV.

## II. METHOD

### A. DEM-based hybrid model

The solid phase is modeled as a collection of discrete particles of "soft" monodisperse spheres (the deformation is accounted for by overlaps), whose individual trajectories are computed by integrating classical equations of motion. Such an approach is often referred to as the soft-sphere molecular dynamics simulation or the discrete element method (DEM). When a pair of objects (particles or system boundaries) get into contact with each other, the interaction force is analyzed in the normal and tangential directions separately,  $F_{\text{cont}} = (F_n; F_s)$ . We adopt the so-called spring-dashpot model of Cundall and

Strack [18], using a Hookean spring

$$F_n = (k_n \delta_n - \gamma v_n) \hat{n}; \quad (1)$$

$$F_s = \text{sign}(v_s) \min(k_t \delta_s; \beta F_n) \hat{s}; \quad (2)$$

where  $k_n$  is the spring stiffness in the normal direction ( $\hat{n}$  is the corresponding unit vector, pointing from the contact point toward the particle center);  $\delta_n$  is the overlap of the particles in the normal direction;  $\gamma$  is the damping coefficient determined by  $k_n$  and the normal coefficient of restitution  $e$  characterizing the inelastic kinetic energy loss upon contact; and  $v_n$  is the normal component of the relative velocity at contact. The interaction in the tangential direction is modeled by a spring and a slider, where the tangential stiffness  $k_t$  is determined by  $k_n$  and the Poisson's ratio of the material  $\nu_p$  [a value of 0.3 is used for all the computations in our study;  $k_t = 2k_n(1 - \nu_p) = (2 - \nu_p)k_n$ ];  $\delta_s$  is the tangential displacement from the initial contact;  $v_s = v_s \hat{s}$  is the tangential component of the relative velocity at contact [ $v_s = \hat{n} \cdot (v_{i,j} - v_j) \hat{n}$ ]; and  $\hat{s}$  is the unit vector in the tangent plane collinear with the component of the relative velocity at contact. The total tangential force is limited by the Coulomb frictional force  $\beta F_n$ , where  $\beta$  is the coefficient of friction. More details on the model equations can be found elsewhere [19].

The equation of motion for each particle accounts for the gas phase effects following the volume-averaged hydrodynamics [20, 21, 22]:

$$m_p \frac{dv_p}{dt} = m_p g + F_{\text{cont}} + F_c + \frac{V_p}{V_g} (\rho_g - \rho_p) (u_g - v_p) - V_p r_p; \quad (3)$$

where  $m_p$  and  $v_p$  are individual particle mass and velocity, respectively. The right-hand side includes various forces acting on the particle, the last two terms arising from the gas-solid two-way coupling; the total force acting on the particles due to the fluid is commonly partitioned into the local drag part and the effective buoyant part, as was done here (see e.g., Ye et al. [23]). The

first term is the body force due to gravity, where  $g$  is the gravitational acceleration, and the second term is a fore-mentioned contact force. The third term accounts for the van der Waals cohesive force  $F_c = \frac{A}{12} \frac{r}{s^2} \hat{n}$ , following Hamaker's formula [24] in the limit of  $s \ll r_1 = r_2$  (monodisperse spheres), where  $A$  is the Hamaker constant,  $s$  is the inter-surface distance, and  $r_1$  and  $r_2$  are the (identical) radii of particles undergoing interaction. We avoid the singularity of this formula at contact by introducing a minimum separation distance of 0.4 nm [25], below which the same attractive force is applied; i.e.,  $F_c = m \max[\frac{A}{12} \frac{r}{s^2}; \frac{A}{12} \frac{r}{(r)^2}] \hat{n}$ . The fourth term accounts for the drag force, where  $\beta$  is the interphase momentum transfer coefficient,  $\rho_g$  is the local average gas phase velocity, and  $V_p$  is the individual particle volume. The last term accounts for the hydrodynamic force due to the gradually varying

part of the pressure field, where  $p$  is the local-average gas phase pressure.

In general, the gas phase variables in the last two terms are obtained by simultaneously integrating the balance equations for gas-solid mixtures; however, for the case of 1D incompressible gas phase, Eq. (3) can be significantly reduced by considering the 1D continuity relation:

$$(1 - \epsilon)u_g + u_s = U_s; \quad (4)$$

and the reduced momentum balance equation:

$$0 = (1 - \epsilon)rp + (\epsilon)(u_g - u_g); \quad (5)$$

where  $u_s$  is the coarse-grained particle velocity, and  $U_s$  is the superficial gas flow velocity. After some manipulation [using Eqs. (4) and (5)], Eq. (3) can be reduced to the following one, where gas phase effects appear as additional terms in the individual equation of motion, involving solid phase coarse-grained, continuum variables [19]:

$$m_p \frac{dv_p}{dt} = m_p g + F_{\text{cont}} + F_c + \frac{V_p}{V} (\epsilon)(u_s - v_p) - \frac{1}{(1 - \epsilon)} (u_s - U_s); \quad (6)$$

For the momentum transfer coefficient, we use an empirical expression proposed by Wen and Yu [26]:

$$= \frac{3}{4} C_D \frac{g(1 - \epsilon) \mu_g u_s}{d_p} (1 - \epsilon)^{2.65}; \quad (7)$$

where  $C_D$  is the drag coefficient,  $\rho_g$  is the gas phase mass density, and  $d_p$  is the particle diameter. The drag coefficient proposed by Rowe [27] is employed

$$C_D = \begin{cases} \frac{24}{Re_g} (1 + 0.15 Re_g^{0.687}); & Re_g < 1000; \\ 0.44; & Re_g \geq 1000; \end{cases} \quad (8)$$

where

$$Re_g = \frac{(1 - \epsilon) \rho_g d_p \mu_g u_s}{\mu_g}; \quad (9)$$

and  $\mu_g$  is the gas phase viscosity. We further simplify these formulas using the assumption of  $Re_g \gg 1$ , as we consider only small particles.

## B. Fully periodic box

Traveling waves in a bed of a finite depth (as in experimental systems) are hardly perfectly periodic. In order to eliminate such an imperfection from the wave, we consider an idealized geometry of a fully periodic (in all three directions) small box of height  $L$  which is commensurate with the wavelength in a deep fluidized bed [19]. The periodic boundary conditions for both lateral directions are achieved with the usual geometrical wrapping. In the

direction of gravity, we adopt the following procedure: For the fully fluidized states that we are interested in, the total weight of the bed is supported by the pressure drop, which can be written as

$$P|_{z=0} - P|_{z=L} = \rho_s g_{\text{avg}} L; \quad (10)$$

where  $\rho_s$  is the mass density of the solid phase,  $g = |j|j$  is the acceleration due to gravity, and  $\epsilon_{\text{avg}}$  is the average volume fraction of the bed. Solving Eq. (10) together with the 1D continuity relation Eq. (4) and the momentum balance equation Eq. (5) yields an appropriate value for the superficial gas flow velocity  $U_s$  that fully fluidizes the bed in this small periodic box. We use this value of  $U_s$  in Eq. (6).

## C. Nondimensionalization

Casting Eqs. (6) and (7) in a dimensionless form, using  $\rho_s, d_p, \rho_g d_p, d_p = g$  as characteristic density, length, velocity, and time, one obtains the following nondimensional groups (arrows indicate changes in the notation from dimensional variables to nondimensional variables that will be used henceforth):

$$\begin{aligned} k_n &= \frac{k_n}{\rho_s g d_p^2}; & \text{spring stiffness} \\ U_s &= \frac{U_s}{\rho \frac{U_s}{g d_p}}; & \text{superficial gas flow rate} \\ &= \frac{1}{d_p}; & \text{scaled minimum separation distance} \\ B_o &= \frac{A}{4 \rho_s g d_p^2}; & \text{cohesive Bond number} \\ St &= \frac{\rho_s g^{1=2} d_p^{3=2}}{g}; & \text{Stokes number} \end{aligned}$$

together with nondimensional parameters, namely  $e, \mu, \rho_p$ , and  $L$  the nondimensional bed height. We characterize particles by usual values ( $e = 0.9; \mu = 0.1; \rho_p = 0.3$ ) in experiments, except when we consider "ideal" particles in Figs. 3 and 18. In the following sections, all the results are presented in nondimensional form.

## D. Computation of solid phase continuum variables

Solid phase coarse-grained continuum variables at 1D discrete grid points separated by  $\Delta z$  are computed by distributing the particle mass and momenta values to two nearby grid points using a halo function  $h$  that linearly decreases to zero around the  $i$ th particle located at  $z = z_i$ :

$$h(z; z_i) = \begin{cases} 1 - \frac{|z - z_i|}{\Delta z} & \text{for } |z - z_i| < \Delta z; \\ 0 & \text{otherwise;} \end{cases} \quad (11)$$

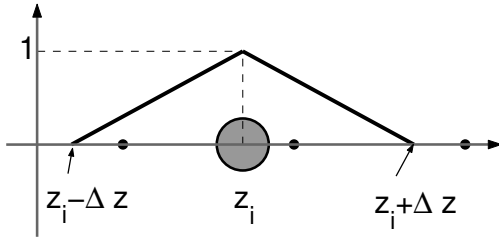


FIG. 1: A schematic of a halo function in Eq. (11), applied to a particle (a large circle) whose center is located at  $z = z_i$ , which is used to compute solid phase coarse-grained continuum variables. Three dots along the abscissa represent nearby grid points. The halo function linearly decreases from the unity at  $z = z_i$  to zero at  $z = z_i \pm \Delta z$ .

where  $z$  is the grid spacing. It is readily seen that  $h$  has the property that the solid phase quantities of each particle are distributed to the two nearby grid points, inversely proportional to the distance to each grid point. The number density  $n$  ( $= \langle \sum_i \delta^3 \rangle$ ) and  $u_s$ , on the grid point  $z_0$  are then defined simply as

$$n(z_0) = \sum_{i=1}^N h(z_0; z_i); \quad (12)$$

$$n(z_0)u_s(z_0) = \sum_{i=1}^N h(z_0; z_i)v_{p,i}; \quad (13)$$

where  $z_i$  is the  $i$ th particle location. Following the same procedure, it is straightforward to compute the granular temperature tensor  $\underline{T}$ :

$$\underline{T} = h(v_{p,i} - u_b) (v_{p,i} - u_b)_i; \quad (14)$$

or the scalar granular temperature  $T = [\frac{1}{D} \text{Tr}(\underline{T})]$ , where  $D$  is the dimensionality,  $\otimes$  is the dyadic tensor product, and  $\text{Tr}$  denotes the trace (of a tensor).

The full stress tensor consists of a kinetic or dynamic part and a virial or static part [28]:

$$\underline{\sigma} = \frac{1}{V} \sum_i m_i \mathbf{v}_{p,i} \mathbf{v}_{p,i} + \sum_{c \in \mathcal{C}} \mathbf{f}_c \otimes \mathbf{l}_c; \quad (15)$$

where  $\mathbf{v}_{p,i} = v_{p,i} - u_b$  is the fluctuating velocity,  $\mathbf{f}$  is the force between contacting particles 1 and 2, and  $\mathbf{l}_c = \mathbf{r}_1 - \mathbf{r}_2$  is the displacement vector between the centers of the particles under consideration. The second term is summed over all the contacts in the averaging volume  $V$ .

Solid phase continuum variables are computed, using the above halo function, on the nodes separated by the grid spacing  $z$ . In order to compute smoothly varying continuum variables across a bed, this procedure is repeated on many subgrid points in between the grid points, by translating all the nodes by a small

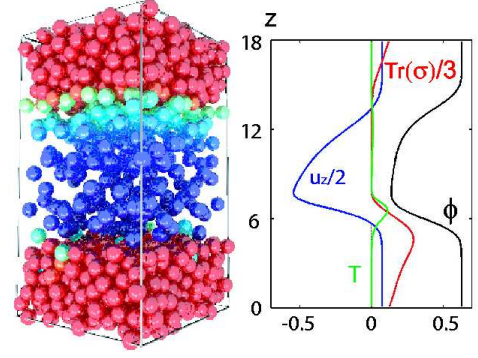


FIG. 2: (Color online) Left panel: A snapshot of non-cohesive particles ( $B_o = 0$ ) in a fully periodic (in all three directions) box ( $10 \times 10 \times 18$ ) whose height is commensurate with one wavelength of a one-dimensional traveling wave (left panel). Right panel: Corresponding coarse-grained solid phase continuum variables: local volume fraction  $\phi$ , vertical component of the locally averaged velocity  $u_z$ , granular temperature  $T$ , and the average normal stress  $\text{Tr}(\underline{\sigma})/D$ , where  $D = 3$  is the dimension. [All quantities are dimensionless.]

amount. As a result, all the continuum variables are computed on uniformly distributed points separated by  $z=10$  throughout the bed.

### III. SIMULATION RESULTS

We consider gas-fluidized beds of non-cohesive as well as cohesive particles in fully periodic boxes of a narrow square-shaped  $10 \times 10$  cross sectional area. The height of the box  $L$ , which is the same as the wavelength in a deep fluidized bed, is set to be 18 in most cases; it is varied when we study the effect of the wavelength in Fig. 7. We also set  $St$  at 55 in most cases, except when  $St$  is varied in Fig. 5. Grid spacing for continuum variables  $z$  is set to be 1.5 in all the computations we will present. We have checked that the quantitative results slightly vary when a different value is used for  $z$ , but the main results remain the same. We also have confirmed that the results are virtually independent of the cross sectional area [19].

We obtain smooth wave profiles by transforming the bed to the co-traveling frame (with the wave), and averaging continuum variables over hundreds of snapshots of fully-developed waves at different instances (as well as spatial smoothing through the halo function). When beds of cohesive particles are considered (Sec. III C), we characterize the level of cohesion by the cohesive Bond number  $B_o$ , which is defined to be the ratio of the maximum cohesive force (at contact) to the gravitational force acting on the particle, namely the weight of the particle.

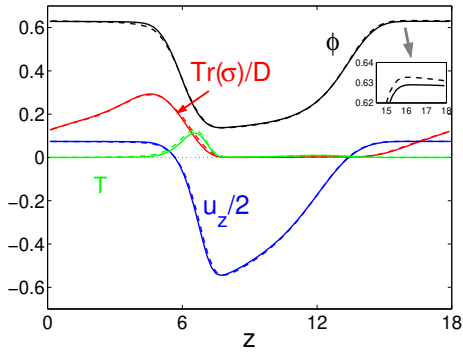


FIG. 3: (Color online) Continuum variable profiles across fully developed waves formed in beds of "realistic" particles (solid lines:  $e = 0.9$ ;  $\mu = 0.1$ ) and of "ideal" particles (dashed lines:  $e = 1.0$ ;  $\mu = 0.0$ ), where  $\phi_{avg}$  is set to be 0.44 for both cases; there are only slight differences between the two cases. The wave travels from left to right, and gravity is acting toward the negative  $z$ -direction. ( $Bo = 0$ ;  $St = 55$ ;  $k_n = 2.0 \cdot 10^5$ .) [All quantities are dimensionless.]

#### A. Traveling planar waves

When beds are subject to a superficial gas flow velocity above the minimum fluidization rate ( $U_s > U_{mf}$ ), homogeneously expanded states are often unstable, and beds form inhomogeneous structures, such as bubbles [6]. In beds of narrow cross sectional areas, bubbling occurs in the form of propagating planar waves (or 1D-TW) of voidage [29], which are reproduced in our model. A snapshot of a bed of non-cohesive particles, forming 1D-TW, illustrates that particles in the upper plug "rain down" through the void region, and accumulate at the top of the lower plug. As a result, the void region propagates up (Fig. 2; red particles are moving up and blue ones are moving down, in online color figure). We use the aforementioned half function (spatial smoothing) and time averaging, to compute the corresponding continuum variables, which are shown in the right panel. For notational convenience, we drop a subscript of  $u_s$  to represent the coarse-grained solid phase velocity by  $u$  (and represent its  $z$ -component by  $u_z$ ).

We start by varying the particle dissipation parameters ( $e$  and  $\mu$ ) to probe the sensitivity of the wave profiles to them. Our simulations reveal that the wave profiles hardly change with the dissipation parameters (Fig. 3). As the particles become more frictional, the plateau volume fraction values in the plug get smaller, since frictional particles pack more loosely in the lower plug because of frictional resistance to rotations (see an inset in Fig. 3). However, the change is very small, because the inertia of the particles is much larger than that of the fluid in gas-fluidized beds (hence particles accumulate with larger velocities, compared to those in liquid-fluidized beds). It is expected that the effect would be more pronounced for smaller particles. Li and

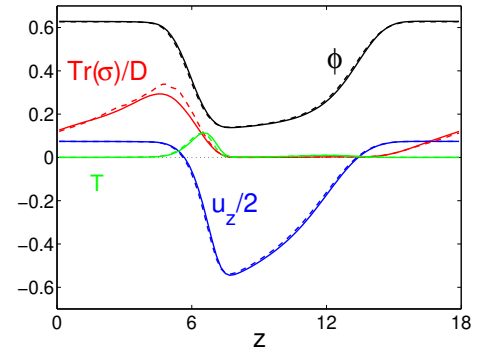


FIG. 4: (Color online) Continuum variable profiles across fully developed waves formed in beds of two types of particles with different stiffness (solid lines:  $k_n = 2.0 \cdot 10^5$ ; dashed lines:  $k_n = 2.0 \cdot 10^8$ ), where  $\phi_{avg}$  is set to be 0.44 for both cases; only slight differences between the two cases. The integration time stepsize for the case of  $k_n = 2.0 \cdot 10^5$  is larger by a factor of 30. ( $e = 0.9$ ;  $\mu = 0.1$ ;  $Bo = 0$ ;  $St = 55$ ;  $\phi_{avg} = 0.44$ .) [All quantities are dimensionless.]

Kuipers [30, 31] showed that heterogeneous structures do exist in "ideal" particles ( $e = 1.0$ ,  $\mu = 0.0$ ), and that dissipative collisions dramatically intensify the heterogeneity of the structures. We do not see such dramatically increased effects; the waveform changes only slightly, which suggests that the wave mainly arises from the instability associated with the interplay between solid phase inertia and the nonlinear volume-fraction-dependent gas drag, as argued by Jackson [32]. Inelastic collisions themselves indeed lead to inhomogeneous structures through a well-known "clustering instability" [33]; however, our simulation suggests that this is a secondary effect in the formation of 1D-TW.

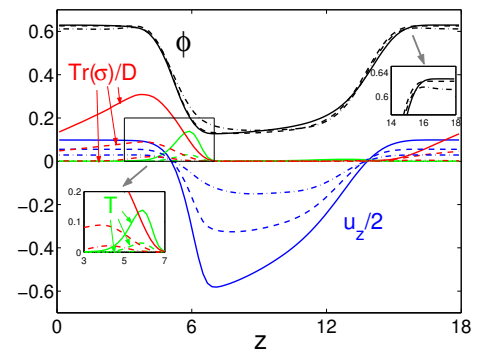


FIG. 5: (Color online) Continuum variable profiles across fully developed waves (of the same wavelength), formed in beds of non-cohesive particles ( $Bo = 0$ ;  $e = 0.9$ ;  $\mu = 0.1$ ;  $\phi_{avg} = 0.36$ ) at different Stokes numbers ( $St = 55$  for solid lines; 28 for dashed lines; 14 for dot-dashed lines). Volume fraction profiles are nearly the same for the three cases, while all the other variables decrease in magnitude, as  $St$  decreases. [All quantities are dimensionless.]

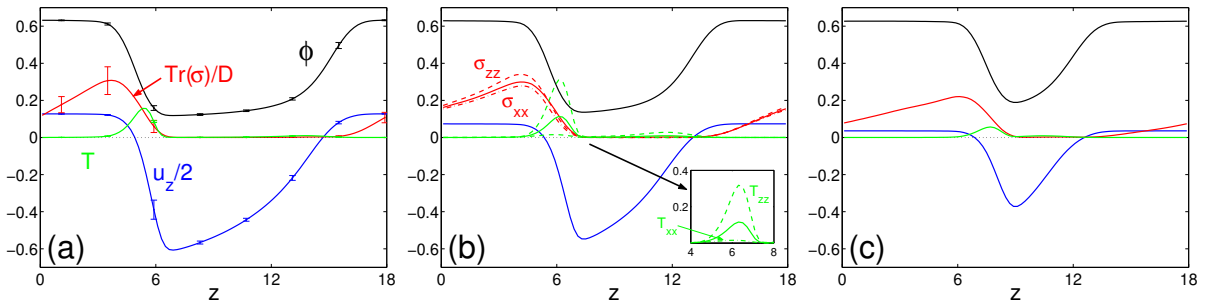


FIG. 6: (Color online) Profiles of solid phase continuum variables for fully developed waves formed in beds of non-cohesive particles ( $Bo = 0; St = 55; e = 0.9; \mu = 0.1$ ) in a fully periodic box of  $10 \times 10 \times 18$ , shown for three cases of different average volume fractions (a)  $\phi_{avg} = 0.36$ ; (b)  $\phi_{avg} = 0.44$ ; (c)  $\phi_{avg} = 0.52$ . Vertical bars in (a) represent the standard deviation of time-averaged data (over 500 snapshots). Different diagonal components of the stress tensor  $\sigma_{xx}$  (dot-dashed line) and  $\sigma_{zz}$  (dashed line) (and those of the granular temperature tensor in inset) are shown separately in (b). [All quantities are dimensionless.]

One ad hoc value used in our simulation is the spring stiffness  $k_n$  (as is the case in most other DEM simulations). In principle, it can be computed from the Young's modulus of the material under consideration; however, such values limit the integration step to extremely small sizes, which leads to expensive computations. We used two values of  $k_n$  differing by three orders of magnitude (while all the other parameters are kept the same), and compared the solid phase continuum variables (Fig. 4). We find that the results are nearly the same, except that the average normal stress  $\text{Tr}(\underline{\underline{\sigma}})/D$  is somewhat larger when a stiffer spring constant value is used; however, the difference in the stress for the two cases is smaller than its level of fluctuation [which is shown later in Fig. 6 (a)]. For the parameters used in Fig. 4, the duration of head-on collision  $t_c = \frac{1}{v} \left( \frac{k_n}{m} \right) \left( 1 + \frac{1}{2} \right)$ , where  $m$  is the reduced mass and  $v = \log e$ , corresponds to  $8.2 \times 10^6$  sec and  $2.6 \times 10^7$  sec for  $k_n = 2.0 \times 10^6$  and  $2.0 \times 10^9$ , respectively; it is reasonably small even for the smaller value of  $k_n$ . For all the rest of the computations, we will use the smaller  $k_n$  value ( $10^6$ ), as it allows us to use an integration timestep size ( $10^2 t_c$ , which scales with  $k_n^{1/2}$  as shown above) larger by a factor of 30.

For the wave profiles shown in Figs. 3 through 7, 12, and 14, the gravity is acting leftward (cf. right panel in Fig. 2). In sustained traveling waves, particles in the upper plug rain down through the void region, and the waves travel to right. In the rest of the paper, we will refer the region where particles fall off from the bottom of upper plug (characterized by  $du_z = dz > 0$ ) as the dilation region, and where the particles accumulate at the top of lower plug ( $du_z = dz < 0$ ) as the compaction region. Let us track the particle phase continuum variables along the direction of gravity, starting from the dilation region: Both the granular temperature and the particle phase stresses are negligibly small across the void region. As a stream of particles collide with the lower plug (in the compaction region), both  $T$  and the stress rapidly increase. The particles quickly become solid-like in the compaction region

through collisional dissipation, and  $T$  starts to decrease (before the stress does). The collisional stress becomes dominant, and it keeps increasing until the volume fraction reaches its plateau value. Inside a plug the stress monotonically decreases, as particles gradually lose contacts and eventually fall off.

Before analyzing the wave profiles any further, we compare them at different Stokes numbers by varying the gas phase viscosity (Fig. 5). For a fixed wavelength, the volume fraction profiles change only slightly; as  $St$  decreases (by increasing  $\eta_g$  by factors of 2 and 4), the plateau value decreases and the overall profile gets smoothed a little bit. More pronounced gas drag makes the magnitude of all other solid phase quantities decrease by comparable factors. Quantitative changes in variables (volume fraction, granular temperature, and average normal stress) are better shown in insets of Fig. 5. We will set  $St = 55$  for the rest of the computations, which corresponds to simulating with usual air.

The volume fraction profiles for a range of average volume fraction  $\phi_{avg}$  [Fig. 6 (a) through (c)] illustrate that the plateau values in the close-packed regions remain nearly the same, while both the depth (wave amplitude) and the width of the void region gradually decrease with increasing  $\phi_{avg}$  (when the wavelength is kept the same). Both the solid phase average normal stress in the compaction region (at the top of the lower plug) and the maximum average speed, decrease as  $\phi_{avg}$  increases. It is worth noting that the solid phase pressure exhibits large fluctuations, whereas all the other variables ( $\phi$ ,  $u$ , and  $T$ ) exhibit relatively small fluctuations [Fig. 6 (a)]. In all cases, in the compaction region, the  $zz$ -component of the stress tensor is larger than the other components ( $xx$ - and  $yy$ -) which are the same due to symmetry [it is shown only in Fig. 6 (b)]. The observed fluctuations of the stress are quantitatively comparable with the difference between  $\sigma_{zz}$  and  $\sigma_{xx}$ ; however, the difference is observed consistently in average quantities for all cases. The anisotropy is significantly large in the granular tem-

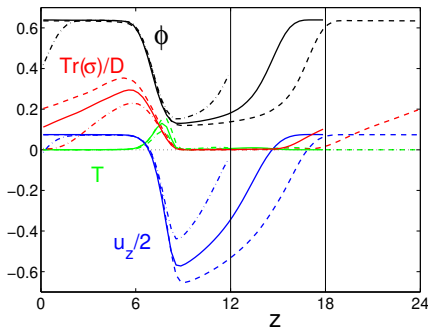


FIG. 7: (Color online) Continuum variable profiles across fully developed waves of different wavelength ( $\lambda = 12$  for dot-dashed lines; 18 for solid lines; 24 for dashed lines), formed in beds of non-cohesive particles ( $e = 0.9$ ;  $\mu = 0.1$ ;  $B_0 = 0$ ;  $St = 55$ ;  $\phi_{avg} = 0.44$ ). The plateau volume fractions remain the same, while the amplitudes of the volume fraction profiles decrease as  $\lambda$  decreases. Vertical thin solid lines at  $z = 12$  and  $18$  represent the system boundaries for the cases of the same wavelengths. [All quantities are dimensionless.]

perature tensor  $\underline{T}$  [see an inset in Fig. 6 (b)], but it is limited to a narrow region in space. The first normal stress difference in sheared granular flows is shown to be a Burnett order effect [34]. However, the normal stress difference that we observe in a bubbling fluidized bed has a different origin (see Appendix for details).

The continuum variables for waves of different wavelengths, for a fixed value of average volume fraction, are shown in Fig. 7. Once the wavelength is sufficiently long, the same plateau volume fraction values are obtained for all three cases. Solid lines in Fig. 7 correspond to the data in Fig. 6 (b). From Figs. 6 and 7 we see that the plateau volume fraction values are the same for ranges of average volume fractions and wavelengths. This is precisely what Glesser et al. [7] obtained in their simulations of continuum models. In their analysis, as the wavelength was decreased, the amplitude of the wave (i.e. of the volume fraction) decreased to zero and the uniform state became stable at a Hopf bifurcation point. We simulate the waves for a range of wavelengths, and compute amplitudes of volume fraction profiles (Fig. 8). Our analysis yields similar results to those which were obtained in the continuum model, but the amplitudes at small wavelengths are finite and the bifurcations are in perfect because of the discrete nature of the model. No further resolution of the data at larger wave numbers is available, as the wavelength increases discretely by  $z (= 1.5)$  (i.e.  $\lambda = 4.5$  and  $6.0$  were used).

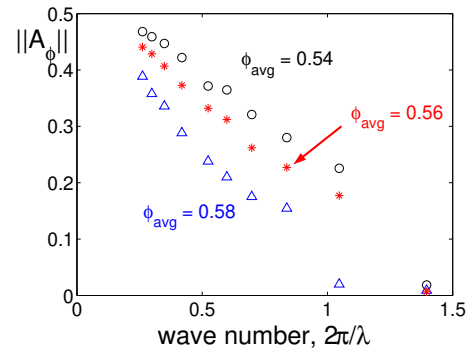


FIG. 8: The wave amplitudes (of the volume fraction profiles) obtained for various wavelengths (4.5 to 24) at three different average volume fractions. ( $\phi_{avg} = 0.54, 0.56, \text{ and } 0.58$ ;  $e = 0.9$ ;  $\mu = 0.1$ ;  $B_0 = 0$ ;  $St = 55$ .)

## B. Particle phase stresses and viscosities, and path dependence

We use the data in Fig. 6 to computationally obtain constitutive relations, and assess consistency with the assumptions used in the KTGM, which is widely used for two-fluid models [3, 4].

We start by plotting the scalar granular temperature  $T$  and average normal stress  $\frac{1}{D}\text{Tr}(\underline{T})$  against the volume fraction for the three cases in Fig. 6 [see Figs. 9 (a) and (b)]; in (b), the volume fraction in the plateau region remains the same for a range of solid phase stresses, and the exact distinction between dilation and compaction branches in this region is elusive]. The computed values in the dilation region are nearly the same for all three cases; however, those in the compaction region strongly depend on  $\phi_{avg}$ . Furthermore, they are significantly different from (and much larger than) those in the dilation region. It is clear that both  $T$  and  $\frac{1}{D}\text{Tr}(\underline{T})$  lie on two distinct branches, depending on where the measurements of these variables are made. Similar "path dependence" was also observed in lattice-Boltzmann simulations of liquid-fluidized beds [35].

In the previous section, we have shown that the granular temperature tensor manifests significant anisotropy, which has to be accounted for, in principle, in our analysis. However, an appreciable anisotropy is seen only in small portion of the compaction region [see inset of Fig. 6 (b)], while the anisotropy [Fig. 6 (b)] and path dependence [Fig. 9 (b)] in the stress tensor are manifest over a wider region. Thus, it is reasonable to believe that neither the anisotropy nor the path dependence of the stress arise from the anisotropy of the granular temperature. Therefore, in what follows, we consider only the scalar granular temperature.

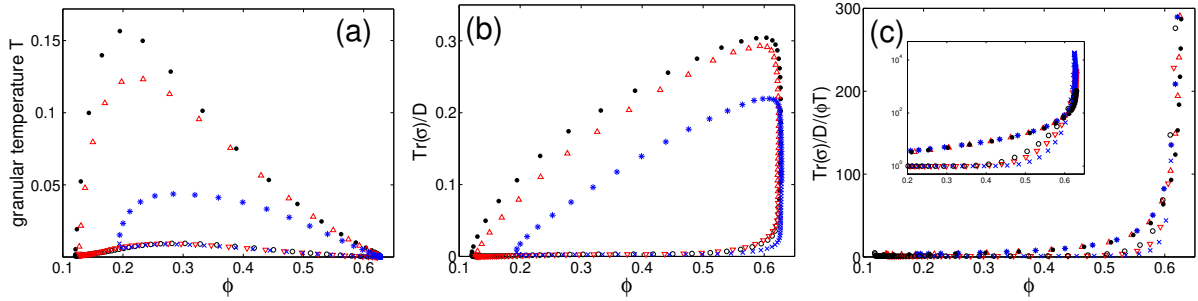


FIG. 9: (Color online) (a) The granular temperature, (b) average normal stress, and (c) average normal stress divided by the solid volume fraction and the temperature (i.e. the unity plus inelastic dense gas correction in the equation of state) for the three cases in Fig. 6 ( $\bullet$ ;  $\triangle$ :  $\phi_{\text{avg}} = 0.36$ ;  $\star$ :  $\phi_{\text{avg}} = 0.44$ ;  $\times$ :  $\phi_{\text{avg}} = 0.52$ ). Measurements from the compaction region where particles accumulate (characterized by  $du_z/dz < 0$ ) are distinguished from those from the dilation region where particles rain down ( $du_z/dz > 0$ );  $\triangle$  and  $\star$  are obtained from the compaction regions, and  $\bullet$  and  $\times$  are obtained from the dilation regions. The same symbols will be consistently used through Fig. 13, and all quantities are dimensionless.

For 1D flows:

$$\frac{1}{D} \text{Tr}(\underline{\underline{\sigma}}) = p_s - \zeta_b \frac{du_z}{dz}; \quad (16)$$

where  $p_s$  is the dimensionless solid phase pressure, and  $\zeta_b$  is the dimensionless bulk viscosity. According to KTGM,

$$p_s = T [1 + 2(1 + e) g_0(\phi)]; \quad (17)$$

where  $g_0(\phi)$  is the isotropic "equilibrium" radial distribution function (RDF) evaluated at contact. We expect that a part of the path dependence of  $\frac{1}{D} \text{Tr}(\underline{\underline{\sigma}})$  arises from the path dependence of  $T$ . We examine whether the first term in Eq. (16) alone (i.e. neglecting the bulk viscosity effect) is enough to explain the path dependence of the stress. We rescale the average normal (dimensionless) stress by  $T$  in Fig. 9 (c), which corresponds to the inelastic and dense gas correction (plus unity) in KTGM, assuming that the relation in Eq. (17) holds. We find that the path dependence still persists. Therefore, Eq. (17) cannot adequately explain the path dependence.

Physically, the path dependence of the average normal stress can be rationalized as follows: As a granular assembly gets diluted or compacted, the RDF at contact departs from its equilibrium value, and depends on the rate of dilation/compaction. When the relevant dimensionless group,  $\frac{du_z}{dz} = \frac{v}{T}$ , is negligibly small, the assembly equilibrates quickly and remains close to the equilibrium configuration. (Note that, in this study, all the results are presented in terms of dimensionless quantities. Since we use the particle diameter as the characteristic length, this dimensionless group becomes  $\frac{du_z}{dz} = \frac{v}{T}$  when  $u_z$ ,  $z$ , and  $T$  are all dimensionless. In terms of dimensional variables, this group would be  $\zeta_b \frac{du_z}{dz} = \frac{v}{T}$ .) However, when this quantity is somewhat larger, the RDF at contact is expressed as a perturbation from its equilibrium value, and the bulk viscosity term accounts for the departure from the equilibrium value. [In such a perturbation approach,

$g_0$  in Eq. (17) will be the equilibrium value and is only a function of particle volume fraction.] Therefore, there is some rationale in trying to explain the path dependence as the effect of the bulk viscosity.

We ascertain that the actual RDF at contact is indeed path-dependent by directly computing it from our simulations. The isotropic RDF at distance  $r = r_n$  is [36]:

$$g(r_n) = \frac{N_{\text{shell}}}{n_{\text{avg}} 4 r_n^2 r}; \quad (18)$$

where  $r_n = (n-1)r$ ,  $n_{\text{avg}}$  is the average number density, and  $N_{\text{shell}}$  is the number of particles lying in a thin spherical shell bounded by  $(n-1)r$  and  $n r$ . We compute the first five values of the RDF ( $1 \leq n \leq 5$ , using  $r = 10^{-2}$ ), and extrapolate them to estimate its value at contact  $r = 0.5$  (Fig. 10); for the sake of better

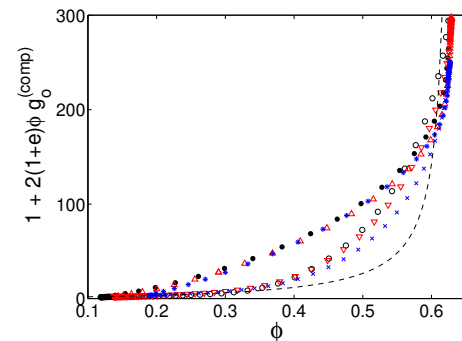


FIG. 10: (Color online) Computationally obtained isotropic RDF at contact (see text for details), for the three cases in Fig. 9, which are appropriately scaled for a better comparison with Fig. 9 (c). The RDFs indeed exhibit path dependence. The dashed line is a scaled plot of an analytical formula used by Bagnold,  $g_0(\phi) = 1/[1 - (\phi - \phi_{\text{max}})^{1-3}]$ , where  $\phi_{\text{max}} = 0.63$  ( $\phi_{\text{max}}$  the plateau volume fraction value) was used.

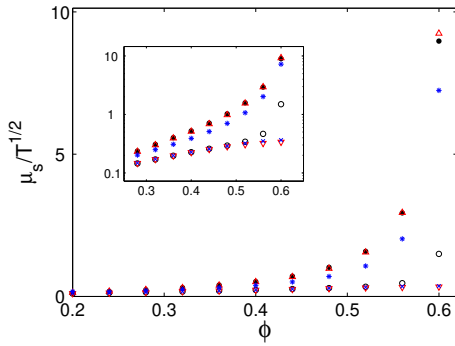


FIG. 11: (Color online) Solid phase dimensionless shear viscosity scaled by dimensionless  $T$ , obtained for the three different values of  $\langle \text{avg} \rangle$  in Fig. 9. Insets include the viscosities shown in linear-logarithmic scale.

comparison with the results in Fig. 9 (c), a prefactor of  $2(1 + e)$  is multiplied and unity is added. The results vary a little bit depending on the choice of  $r$  and the extrapolation method. However, in all cases, the path dependence persists. Thus we can indeed expect a non-negligible bulk viscosity correction. Before discussing the bulk viscosity effect, let us look at the shear viscosity.

We numerically estimate the first derivative of the average velocity fields through the central differencing scheme, and compute the effective (dimensionless) shear viscosity  $\mu_s$  from different components of the stress tensor:

$$\mu_s = \frac{1}{D} \text{Tr}(\underline{\underline{\sigma}}) = \frac{4}{3} \mu_s \frac{du_z}{dz} \quad (19)$$

As the shear viscosity in KTGM depends on  $T$ , we plot  $\mu_s$  after rescaling it by  $T$  (Fig. 11). We find that scaled  $\mu_s$ 's computed from different  $\langle \text{avg} \rangle$ 's collapse nearly onto common functional forms, but the path dependence is very clear. In the KTGM, the shear viscosity has no path dependence [4]:

$$\mu_s = \frac{5^D}{48(1+e)g_0} \left( 1 + \frac{4}{5}(1+e)g_0 \right)^2 + \frac{4}{5} g_0^2 (1+e) \frac{r}{T}; \quad (20)$$

which holds, again, for small magnitude of  $\frac{du_z}{dz} = \frac{P}{T}$ , and the apparent path dependence again signals clearly a marked departure from conditions assumed in the development of KTGM.

We have computed the dimensionless quantity  $\frac{du_z}{dz} = \frac{P}{T}$  from our simulation results; see Fig. 12. Note that the magnitude of this quantity is not small compared to unity, and so the assumption that the actual RDF at contact can be written as a small perturbation from the equilibrium value, which is routinely made in the theories, does not hold in this rather simple inhomogeneous flow.

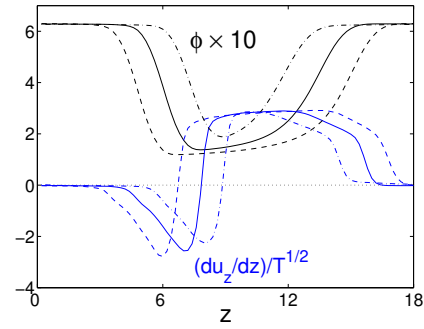


FIG. 12: (Color online) A dimensionless group relevant to the rate of dilation or compaction,  $\frac{du_z}{dz} = \frac{P}{T}$ , for the cases in Fig. 6 (dashed lines:  $\langle \text{avg} \rangle = 0.36$ ; solid lines:  $\langle \text{avg} \rangle = 0.44$ ; dot-dashed lines:  $\langle \text{avg} \rangle = 0.52$ ), plotted together with the scaled volume fraction profile. [Here  $z$ ,  $u_z$ , and  $T$  are all dimensionless.]

The path dependence of the shear viscosity is thus clearly associated with effects which are nonlinear in  $\frac{du_z}{dz} = \frac{P}{T}$ .

Having found that  $\mu_s$  is path-dependent, we can expect the bulk viscosity  $\mu_b$  to differ in the compaction and dilation branches as well. Strictly speaking, there is no unique way of partitioning  $\frac{1}{D} \text{Tr}(\underline{\underline{\sigma}})$  into  $\mu_s$  and  $\mu_b \frac{du_z}{dz}$ , if  $\mu_b$  is going to depend on  $\mu_s$ ,  $T$ , and the path. However, it is clear from Fig. 9 that  $T$  and  $\frac{1}{D} \text{Tr}(\underline{\underline{\sigma}})$  in the dilation branch are nearly identical for the three cases, and independent of  $\frac{du_z}{dz} = \frac{P}{T}$ . This suggests that the bulk viscosity in the dilation branch is close to zero, so that  $\frac{1}{D} \text{Tr}(\underline{\underline{\sigma}})$  in the dilation branch can be taken as simply equal to  $\mu_s$  in that branch. As seen in Fig. 11, the shear viscosity in the dilation branch is much smaller than that in the compaction branch. Thus, it is not unreasonable to suspect that the bulk viscosity correction in the dilation branch is small:

$$\mu_b \frac{du_z}{dz} \approx \frac{1}{D} \text{Tr}(\underline{\underline{\sigma}}) \Big|_{\text{dil}};$$

where the subscript dil indicates evaluation on the dilation branch. Armed with this, we can estimate the bulk viscosity in the compaction branch in at least two different ways. First, we can set (assume)  $\mu_b \Big|_{\text{dil}} = \mu_b \Big|_{\text{comp}}$  and write

$$\frac{1}{D} \text{Tr}(\underline{\underline{\sigma}}) \Big|_{\text{comp}} = \frac{1}{D} \text{Tr}(\underline{\underline{\sigma}}) \Big|_{\text{dil}} + \mu_b \frac{du_z}{dz} \Big|_{\text{comp}}; \quad (21)$$

where the subscript comp indicates evaluation on the compaction branch. Bulk viscosity values in the compaction branch estimated in this manner are shown in Fig. 13 (a). Alternately one can recognize that the granular temperature is different in the two branches; ac-

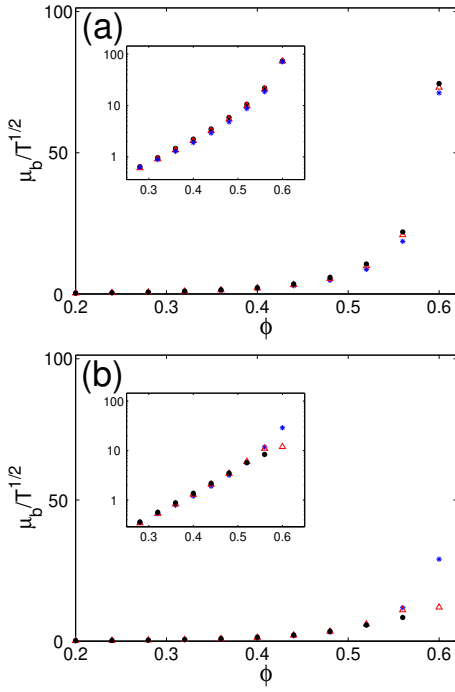


FIG. 13: (Color online) Solid phase dimensionless bulk viscosity scaled by dimensionless  $T$ , obtained for the three different values of  $\phi_{avg}$  in Fig. 9, estimated via (a) Eq. (21), and (b) Eq. (22). Insets include the viscosities shown in linear-logarithmic scale.

counting for the difference, we can write

$$\frac{1}{D} \text{Tr}(\underline{\underline{\tau}})_{\text{comp}} = \frac{1}{D} \text{Tr}(\underline{\underline{\tau}})_{\text{dil}} \frac{T_{\text{comp}}}{T_{\text{dil}}} \quad \text{b} \frac{du_z}{dz} \text{comp} : \quad (22)$$

Figure 13 (b) shows the bulk viscosity values estimated via Eq. (22). In both Figs. 13 (a) and (b), the bulk viscosity values are scaled by  $T_{\text{comp}}$ . The insets in these figures show the results in a linear-logarithmic scale. The second approach leads to smaller estimates for the bulk viscosity. However, it is clear that irrespective of the approach (assumption) taken [i.e. Eq. (21) or (22)], the estimated values of bulk viscosity in the compaction branch are found to be appreciably larger than the shear viscosity (compare Figs. 11 and 13). It is interesting to contrast this with KTG predictions [4]:

$$\text{b} = \frac{4}{3} \tau_0^2 g_0 (1 + e) \frac{\tau}{T} \quad (23)$$

which is smaller than the magnitude of the shear viscosity.

It should be emphasized that the 1D-TW studied here is not a peculiar problem representing extreme conditions. Such sharp volume fraction gradients routinely occur around bubble-like voids and clusters in fluidized

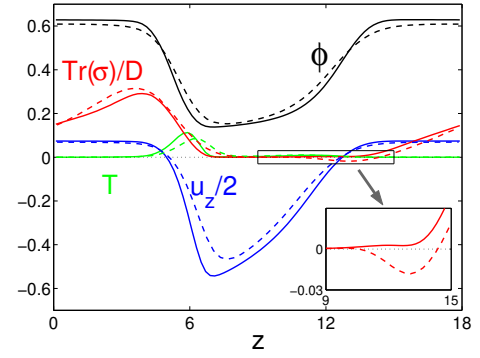


FIG. 14: (Color online) Profiles of solid phase continuum variables obtained for non-cohesive ( $B_o = 0$ , solid lines) and slightly cohesive ( $B_o = 2$ , dashed lines) particles, with the same average volume fraction,  $\phi_{avg} = 0.44$ . The inset shows a blow-up of the region where the stress of the cohesive bed becomes tensile. ( $e = 0.9$ ;  $\mu = 0.1$ ;  $St = 55$ .)

beds, turbulent beds, and fast fluidized beds [38]. In such devices, the particle assembly is frequently subjected to local dilation and compaction in alternating manner. In these flows,  $\text{div} \underline{\underline{\tau}} = T \underline{\underline{m}}$  may not be small and this can lead to the type of effects seen in this study.

### C. Effect of cohesion

It is well known that beds of fine powders are difficult to fluidize because of the cohesive force between the particles. Beds of cohesive powders have attracted increased attention in recent years; however, their theoretical understanding is still limited. In this section, we vary the level of cohesion to probe how the cohesive force changes the wave profiles and the relations among continuum variables.

The waves formed in beds of weakly cohesive particles ( $B_o < 2$ ) retain a virtually invariant shape over time, and travel with a well-defined constant speed. They become more and more irregular and slow down, until they vanish at  $B_o \approx 8$ , depending on  $\mu$  and  $\phi_{avg}$ ; the propagation speed at  $B_o = 6$  (3) is about 60% (85%) of that in beds of  $B_o = 0$  [19]. The wave profiles for non-cohesive and weakly cohesive particles ( $B_o \leq 2$ ) are shown in (Fig. 14). There are two major differences between the waves in beds of non-cohesive and of cohesive particles: Firstly, the plateau volume fraction is smaller in cohesive beds, as cohesive particles pack more loosely than non-cohesive ones, due to reasons similar to those for frictional particles (See e.g., Dong et al. [39]). Even for slightly cohesive particles, this effect is appreciable (see inset of Fig. 14); i.e. the effect is more pronounced compared to that of a changing friction coefficient (Fig. 3). Secondly, the average normal stress becomes tensile and remains so for a certain range of the height in the dilation region. At the bottom of the upper plug, the average

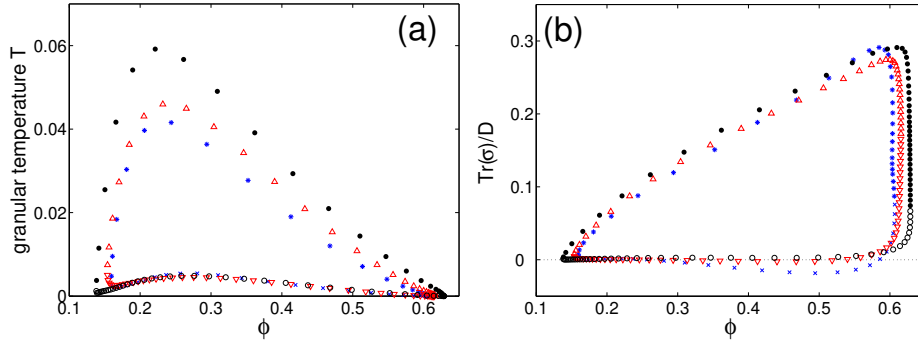


FIG .15: (Color online) Solid phase granular temperature and average normal stress for three cases of different cohesion level ( $\bullet$ ;  $\triangle$ :  $B_o = 0$ ;  $\square$ :  $B_o = 1$ ;  $\circ$ :  $B_o = 2$ );  $\phi_{\text{avg}} = 0.44$  in all cases ( $e = 0.9$ ;  $\mu = 0.1$ ).  $\bullet$ ;  $\triangle$ ;  $\square$ 's are obtained from the compaction regions, and  $\circ$ ;  $\triangle$ ;  $\square$ 's are obtained from the dilation regions. ( $St = 55$ .) The wave speed monotonically slows down with increasing level of cohesion, until the wave disappears at  $B_o = 8$ ; the wave speed in beds of  $B_o = 2$  is 90% of that in  $B_o = 0$ .

normal stress monotonically decreases until it reaches its minimum value (the largest tensile stress) and the assembly breaks up (inset in Fig. 14). The magnitude of the tensile stress cannot exceed the tensile strength of the cohesive assembly; thus, one can expect that the former corresponds to the tensile strength of this fluidized bed. When we estimate the tensile strength via this reasoning, it is almost an order of magnitude smaller than what is predicted by Rumpf's model [19]. This makes sense, since the cohesive assembly in a fluidized bed breaks up through the direction of the weakest linkage, in contrast to all directions isotropically, as assumed in Rumpf's model [37]. We observe further decrease (increase) of the plateau volume fraction (the magnitude of maximum tensile strength), as  $B_o$  increases, until the waves vanish (i.e. the bed does not get fluidized anymore) at  $B_o = 8$ . The size of agglomerates broken off of the cohesive assembly however has a distribution, and the wave profile

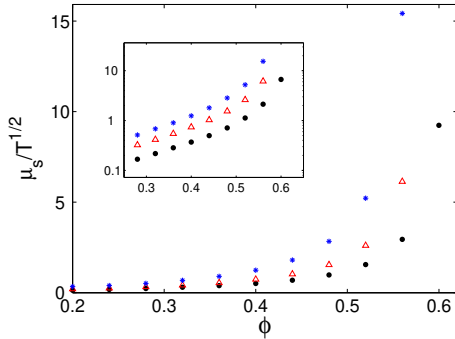


FIG .16: (Color online) Solid phase dimensionless shear viscosity in the compaction branch ( $\phi_{\text{avg}} = 0.44$ ), scaled by dimensionless  $T$ , obtained from the three cases of different values of  $B_o$  in Fig. 15 ( $\bullet$ :  $B_o = 0$ ;  $\triangle$ :  $B_o = 1$ ;  $\square$ :  $B_o = 2$ .) The viscosities are shown in linear-logarithmic scale in the inset.

becomes irregular for  $B_o > 3$ , which makes a quantitative analysis difficult. For sufficiently cohesive particles ( $B_o > 8$ ), as one can readily expect, the maximum tensile stress driven solely by gravity fails to reach the tensile strength of the material, and the bed does not form a stable traveling wave anymore. At that point, an additional mechanism, such as mechanical vibration or the powder coating, has to be implemented to fluidize them [40, 41].

As in the beds of non-cohesive particles, both  $T$  and  $\text{Tr}(\sigma)/D$  form lobes when plotted against  $\phi$ , and manifest the same path dependence (Figs. 15 and 17). Clearly, our arguments on pronounced bulk viscosity effects, and on path dependence of both the bulk and shear viscosities inferred for beds of non-cohesive particles should remain valid for beds of moderately cohesive particles as well. As  $B_o$  increases (in a narrow range of  $B_o \approx 2$ , at a fixed average volume fraction), both the maximum granular temperature [Fig. 15 (a)] and the maximum volume fraction in the plateau region [Fig. 15 (b)] decrease noticeably, but the maximum (compressive) value attained by the average normal stress remains nearly the same. We compute the shear viscosity for the three cases shown in Fig. 15, and find that it increases as  $B_o$  increases (only the values on compaction branches are shown in Fig. 16 for clarity), as one can expect.

For a fixed level of cohesion ( $B_o = 2$ ), the maximum granular temperature decreases as the average volume fraction increases [Fig. 17 (a)], because the void region gets narrower and particles accumulate more gently as in the beds of non-cohesive particles with varying average volume fraction. The average normal stress value for different  $\phi_{\text{avg}}$  in the compaction branch varies. However, the granular temperature [Fig. 17 (a)] and average normal stress [Fig. 17 (b)] in the dilation branch for the three cases follow (roughly) the same curve until the assembly breaks up; as in beds of non-cohesive particles, dilation branches follow nearly the same curves.

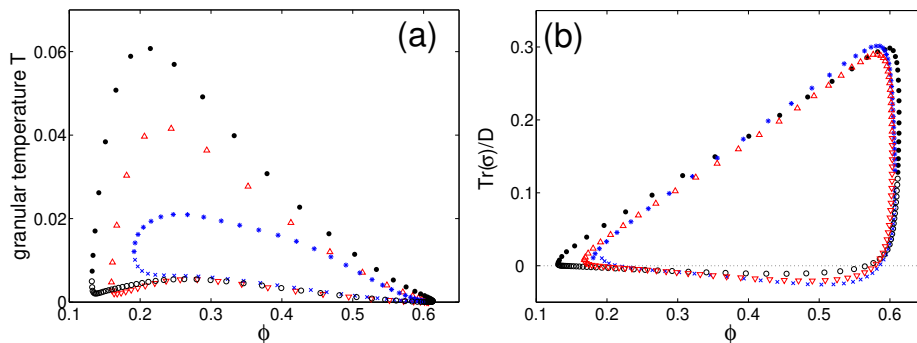


FIG. 17: (Color online) Solid phase granular temperature and average normal stress in beds of cohesive particles ( $B_0 = 2; e = 0.9; \mu = 0.1$ ) for three different average volume fractions ( $\phi$ ;  $\phi_{avg} = 0.40$ ;  $\phi_{avg} = 0.44$ ;  $\phi_{avg} = 0.48$ ).  $\phi_{avg} = 0.40$ ;  $\phi_{avg} = 0.44$ ;  $\phi_{avg} = 0.48$ 's are obtained from the compaction regions, and  $\phi_{avg} = 0.40$ ;  $\phi_{avg} = 0.44$ ;  $\phi_{avg} = 0.48$ 's are obtained from the dilation regions. ( $St = 55$ .)

#### IV. DISCUSSION

Soft sphere models for particle-particle interactions have been used in the literature for nearly three decades to analyze a variety of dense particulate flow problems [15, 18, 42, 43, 44, 45, 46, 47, 48, 49]. The particle dynamics-based hybrid model employed in our study, which combines a soft-sphere model for the particles with local-average equations for the gas phase, has been used previously to simulate flows of gas-particle mixtures [20, 21, 22, 23, 50, 51, 52, 53, 54], including those occurring in multidimensional fluidized beds [20, 21, 22, 23, 52, 53, 54], and successfully compared against experimental data [55, 56]. Thus there is ample basis for using this approach to probe the nature of inhomogeneous gas-particle flows. We have used this model to simulate one of the simplest spatiotemporal structures possible in gas-fluidized beds, namely one-dimensional traveling waves (1D-TW). We believe that such a simple structure is ideal for our study, as it contains both compacting and dilating regions, and its steady nature (in the co-traveling frame) allows us to perform suitable ensemble-averaging, which is essential for the analysis of results of discrete simulations. Through an analysis of "computational data" generated through simulations of these traveling wave structures, we have examined in this study the possible consequences of compaction and dilation rates on the stresses generated in the particle assembly. Such volume changes accompany most gas-particle flows, and understanding their effects on the stresses is thus of practical importance.

It is well established in the literature, through stability analysis based on continuum two-fluid models, that such traveling waves are the most dominant modes through which homogeneously fluidized suspensions lose stability. In real gas-fluidized beds, such traveling waves are not observed, as they quickly give way to a secondary instability leading to bubble-like voids [6, 7, 57]. However, one can readily generate such traveling waves in computations by restricting the cross-section of the bed to only

several particle diameters, thereby suppressing the secondary instability [29]. Although the 1D-TW generated in this manner are artificial structures, they represent a simple, suitable inhomogeneous flow pattern where the particle assembly undergoes compaction and dilation alternately in a periodic manner.

We began by generating computational data on 1D-TW for assemblies of uniformly sized, spherical, non-cohesive particles. We demonstrated that the particle volume fraction profiles observed in the hybrid model calculations are qualitatively similar to those seen previously in analyses of two-fluid models [7, 57]. These traveling waves in dense fluidized beds take the form of vertically rising plugs of particles. The particle volume fraction in the plugs was found to be essentially independent of the average particle volume fraction in the wave, while the height of the void and the lowest volume fraction attained in this void depended systematically on it (see Figs. 6 and 7) — just as in the case of similar structures obtained via two-fluid models supplemented with ad hoc closures [7, 57]. The present hybrid model replaces the ad hoc closures for solid phase stresses in the two-fluid model with particle-particle interaction models.

The variation of wave amplitude with wavenumber (Fig. 8) obtained in our simulations is also similar to that obtained with two-fluid models. Typically, in two-fluid models, the homogeneous state is stable for short wavelengths, and it gives way to traveling waves via a Hopf bifurcation at some critical wavelength. As the wavelength increases further, the wave amplitude increases [7]. Although the discrete simulations undertaken in the present study do not exhibit a perfect bifurcation from a uniform solution to a traveling wave solution, one can readily recognize the correspondence between our discrete simulations and corresponding two-fluid model calculations of Glasser et al. [7].

Our discrete simulations clearly show that the solid phase stresses and the granular temperature obtained by ensemble-averaging over many realizations are path-dependent. We have checked that the normal stress dif-

ference in bubbling fluidized beds is different from the well-known Bunnell order effect in sheared granular fluids (See Appendix). The traveling wave can be partitioned into two regions, one where the assembly undergoes dilation and the other where it undergoes compaction. The solid phase stresses and the granular temperature in these two regions differ markedly (see Fig. 9). While one does expect some difference in the behavior observed in the two regions, our simulations reveal that the difference is much larger than what can be attributed to the bulk viscosity correction in the widely used kinetic theory for granular materials (KTGM). The kinetic theory is limited to situations where the volumetric strain rate is small compared to the rate at which local microstructure equilibrates, so that the effect of the volumetric strain rate can be treated as a small perturbation from the equilibrium microstructure. Our computations show that, in this simple traveling wave, the volumetric strain rate is not small (see Fig. 12). Although these traveling waves are not observed in real gas-fluidized beds, it is such one-dimensional traveling waves that give way to bubble-like voids, and so one can readily expect that the same effects will be observed in bubble-like voids as well.

Large (scaled) volumetric strain rates can be expected to lead to nonlinear effects, and this is indeed seen. Both bulk and shear viscosities in the solid phase are found to depend on the volumetric strain rate (see Figs. 11 and 13), and such dependence is not captured by the KTGM (which only considers the case of small-scale volumetric strain rates). When two-fluid models fail to account for such nonlinear effects, they cannot be expected to reproduce the macroscopic properties of the void region accurately. It is well established that bubble-like voids readily form in two-fluid model calculations even with a simple phenomenological closure for the particle phase stress [4, 7, 57]; however, the shape of such voids is not consistent with those observed experimentally. A part of this problem stems from numerical errors associated with discretization of the two-fluid model equations [58]; however, numerical accuracy is not the sole factor. In the dense emulsion phase in the immediate vicinity of the bubble-like void, one can expect large-scale volumetric strain rates (just as in the 1D-TW examined in this study) and the failure to account for the accompanying nonlinear effects will impact the characteristics of the bubble-like voids.

In many technological applications involving gas-particle flows, particles in the 50 - 100  $\mu$ m size range are employed. Such particles, belonging to Geldart type A [59], manifest modest levels of inter-particle cohesion and the relevance of this cohesive interaction on the flow characteristics has been debated extensively in the literature (for example, see a review article by Sundaresan [6]); however, concrete conclusions are yet to emerge. In the present study, we have also examined the effect of inter-particle cohesion on the structure of the traveling wave. The inter-particle cohesive force model itself is quite simple, but it suffices to explore the generic effects. It is

found that all of the effects observed in non-cohesive systems persist when a modest level of cohesion is added (see Figs. 15 and 17). Cohesion lowers the particle volume fraction in the plateau region and hence the amplitude of the wave. It also slows down the speed of the wave propagation (see caption of Fig. 15) (which in multi-dimensional systems affords greater exchange of gas between the void and the surrounding emulsion). Thus the beneficial effect of modest levels of cohesion can be understood.

Although we have presented results only for  $B_o$  up to 2, we found that wave solutions could be obtained even for larger  $B_o$  values. At larger  $B_o$  values (e.g.,  $B_o = 4$ ), the waves became irregular and when  $B_o > 8$ , the entire assembly traveled as a single plug. This is not a surprising result, as it is well known that highly cohesive particles (Geldart type C [59]) do not fluidize well. Thus the range of  $B_o$  over which beds can be fluidized without additional excitation (such as mechanical vibrations) is  $B_o < 8$ . Since the wave propagation is irregular for  $B_o > 3$ , the narrow range of  $0 < B_o < 3$  is more appropriate for smooth fluidization and hence quantitative analysis through ensemble-averaging. At such levels of cohesion, the particle assembly is clearly in a state of tension when it undergoes dilation (see Figs. 15 and 17). It also clearly speaks for the need to include in two-fluid models a path-dependent model for the granular pressure.

#### Acknowledgments

SJM is grateful to Lee Arons for helpful discussions. This work was supported by grants from The New Jersey Commission on Science and Technology and Merck & Co., Inc., the US DOE, and a Guggenheim Fellowship (IGK).

#### Appendix: The normal stress differences in sheared gas-fluidized beds

Normal stress difference can arise due to Bunnell order effects (Sela and Goldhirsh [34]). Theoretical prediction for normal stress difference attributable to Bunnell order effects is available only for the dilute limit, and a validated Bunnell order hydrodynamic theory for bubbling fluidized beds (i.e. dense suspensions) is currently unavailable. We first estimated the normal stress differences ( $\sigma_{zz} - \sigma_{xx}$ ) using a general relationship provided by Sela and Goldhirsh [34] (even though it was developed for the dilute limit), and then considered a couple of relevant computational experiments in order to probe if the stress differences that we observed in our fluidized beds were consistent with Bunnell order effects.

According to a general Bunnell order expression for the stresses (Eq. (46) in Sela and Goldhirsh [34]), the normal stress difference in 1D-TW in fluidized beds de-

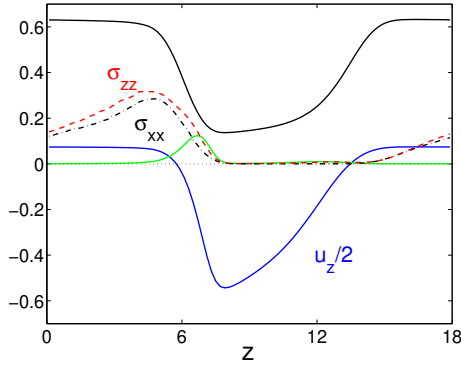


FIG. 18: Solid phase continuum variables of beds of ideal particles ( $e = 1.0$ ;  $\mu = 0.0$ ;  $Bo = 0$ ;  $St = 55$ ;  $\mu_{avg} = 0.44$ ).

depends on (products of) gradients of solid phase continuum variables, such as  $du_z/dz$ ,  $dT/dz$ , and  $d^2T/dz^2$ . We determined that, for the waves in our simulations, the dominant contribution came from a term of the form  $C^{-2}(du_z/dz)^2$ , where  $C$  is a constant of order of unity and  $\lambda$  is the mean free path. In dense suspensions,  $\lambda$  is much smaller than unity. We found this term to be much smaller than the  $(\sigma_{zz} - \sigma_{xx})$  values that we obtained in our simulations (see, for instance, Fig. 6 (b)). Thus, there is no basis for attributing the stress difference seen in our simulations to Burnett order effects.

To test this issue further, we also considered two additional computational experiments:

- (i) The Burnett order theory by Sela and Goldhirsh [34] for homogeneously sheared granular flows in the dilute limit showed that the normal stress differences still persist in the elastic limit. This theory also predicts that the first normal stress difference  $(\sigma_{zz} - \sigma_{xx}) = (Tr(\underline{\underline{\sigma}}) - D)$ , in our case) is a rapidly increasing function of inelasticity. We first computed different diagonal components of the stress in usual fluidized beds, using ideal particles ( $e = 1.0$ ;  $\mu = 0.0$ ) used in Fig. 3, and examined their dependence on the inelasticity.
- (ii) Using dissipative particles ( $e = 0.9$ ;  $\mu = 0.1$ ), we applied homogeneous shear in the  $y$  direction to a fluidized bed; if there were any systematic normal stress difference between the  $xx$  and  $yy$  components, it would be mostly attributed to the Burnett order effects (and/or collisional anisotropy [60]).

In a bed of ideal particles (case (i) above, shown in Fig. 18), a noticeable normal stress difference  $(\sigma_{zz} - \sigma_{xx})$  persists at a level comparable to the dissipative particle system. Comparing the results for the ideal and dissipative systems, we saw that the ratio  $(\sigma_{zz} - \sigma_{xx}) = (Tr(\underline{\underline{\sigma}}) - D)$  was not a strong function of inelasticity. This further confirms that Burnett order effect is unimportant.

When we applied shear to a fluidized bed (case (ii),

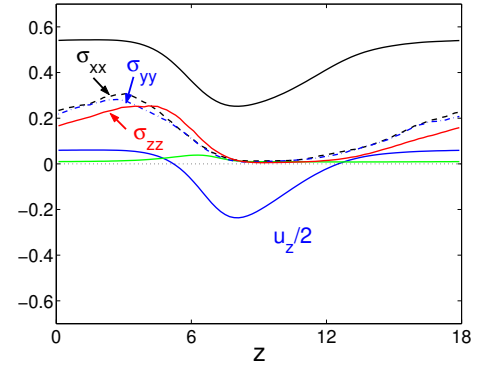


FIG. 19: Solid phase continuum variables in sheared fluidized beds (computed by employing Lees-Edwards boundary condition in the  $y$  direction). The shear strain rate  $du_x/dy$  of 0.2 is applied. ( $e = 0.9$ ;  $\mu = 0.1$ ;  $Bo = 0$ ;  $St = 55$ ;  $\mu_{avg} = 0.44$ ).

shown in Fig. 19) in the  $y$  direction, we still saw significant differences between  $xx$  (or  $yy$ ) and  $zz$  component normal stresses, but those between  $xx$  and  $yy$  components were relatively very small. The maximum volumetric strain rate ( $du_z/dz = 0.2$ ) in Fig. 19 is comparable to the shear strain rate applied ( $du_x/dy = 0.2$ ). When we increased the shear strain rate to 1.0, the bed became homogenized and the region of low particle volume fraction was not visibly recognizable anymore. Sheared gas fluidized beds are known to fluidize homogeneously when the shear rate reaches some critical value, depending on the superficial gas flow rate [61]. Our computation yielded comparable values for the critical shear rate, however, quantitative comparison was not possible, as the critical rate also depends on the bed height [61].

To summarize, we used a Burnett order expression [34] for normal stress differences (which was developed for the dilute limit) to estimate its prediction for dense suspensions (as this is the only available theory). We found that such prediction significantly underestimated normal stress difference seen in our wave simulations. Furthermore, when we assessed the first normal stress difference in beds of perfectly elastic particles, we did not observe any noticeable decrease (from that in beds of inelastic particles). In order to computationally obtain the normal stress difference in sheared dense suspensions (as opposed to dilute granular flows in the absence of gas), we considered a sheared fluidized bed. We found that the normal stress difference between the  $xx$  and  $yy$  components (presumably attributed to Burnett order effects and/or collisional anisotropy) is still much smaller than the difference between the  $xx$  and  $zz$  components which arises from compaction and dilation. Based on all these results, we conclude that  $(\sigma_{zz} - \sigma_{xx})$  seen in our traveling wave simulations is not due to Burnett order effects or collisional anisotropy.

- [1] C. C. Rowe, M. Sommerfeld, and Y. Tsuji, *Multiphase flows with droplets and particles*, (CRC Press, Boca Raton, 1998).
- [2] L. S. Fan and C. Zhu, *Principles of Gas-Solid Flows*, (Cambridge University Press, Cambridge, 1998).
- [3] R. Jackson, *The Dynamics of Fluidized Particles* (Cambridge University Press, Cambridge, 2000).
- [4] D. Gidaspow, *Multiphase Flow and Fluidization: Continuum and Kinetic Theory Description* (Academic Press, Boston, 1994).
- [5] S. B. Savage, "Instability of uniform unbounded granular shear flow," *J. Fluid Mech.* 241, 190 (1992).
- [6] S. Sundaresan, "Instabilities in fluidized beds," *Annu. Rev. Fluid Mech.* 35, 63 (2003).
- [7] B. G. Lasser, I. G. Kevrekidis, and S. Sundaresan, "One- and two-dimensional traveling wave solutions in gas-fluidized beds," *J. Fluid Mech.* 306, 183 (1996).
- [8] S. B. Savage and S. M. Kowen, "Shear stresses developed during rapid shear of concentrated suspensions of large spherical particles between concentric cylinders," *J. Fluid Mech.* 127, 453 (1983).
- [9] C. K. K. Lun, S. B. Savage, D. J. Jeffrey, and N. Chhabra, "Kinetic theories for granular flow: Inelastic particles in Couette flow and slightly inelastic particles in a general flow field," *J. Fluid Mech.* 140, 223 (1984).
- [10] J. T. Jenkins and M. W. Richman, "Grad's 13-moment system for a dense gas of inelastic spheres," *Arch. Ration. Mech. Anal.* 87, 355 (1985).
- [11] D. L. Koch and A. S. Sangani, "Particle pressure and marginal stability limits for a homogeneous monodisperse gas-fluidized bed: kinetic theory and numerical simulations," *J. Fluid Mech.* 400, 229 (1999).
- [12] C. S. Campbell, "Rapid granular flows," *Annu. Rev. Fluid Mech.* 22, 57 (1990).
- [13] K. Agrawal, P. N. Loezos, M. Syamlal, and S. Sundaresan, "The role of meso-scale structures in rapid gas(solid) flows," *J. Fluid Mech.* 445, 151 (2001).
- [14] H. Kim and H. A. Rastopou, "Extension of kinetic theory to cohesive particle flow," *Powder Tech.* 122, 83 (2002).
- [15] M. A. Hopkins and M. Y. Louge, "Inelastic microstructure in rapid granular flows of smooth disks," *Phys. Fluids A* 3, 47 (1990).
- [16] J. S. Curtis and B. van Wachem, "Modeling particle-laden flows: A research outlook," *AIChE J.* 50, 2638 (2004).
- [17] R. Celland and C. M. Henry, "Simulations of a binary-sized mixture of inelastic grains in rapid shear flow," *Phys. Rev. E* 65, 031301 (2002).
- [18] P. A. Cundall and O. D. L. Strack, "A discrete numerical model for granular assemblies," *Geotechnique* 29, 47 (1979).
- [19] S. J. Moon, I. G. Kevrekidis, and S. Sundaresan, "Particle simulation of vibrated gas-fluidized beds of cohesive powders," to appear in *Ind. & Eng. Chem. Res.* A SAP Article DOI:10.1021/ie051114s (2006); also available from <http://arxiv.org/abs/cond-mat/0510115>
- [20] Y. Tsuji, T. Kawaguchi, and T. Tanaka, "Discrete particle simulation of two-dimensional fluidized bed," *Powder Technol.* 77, 79 (1993).
- [21] B. P. B. Hoofmans, J. A. M. Kuipers, W. J. Briels, and W. P. M. van Swaaij, "Discrete particle simulation of bubble and slug formation in a two-dimensional gas-fluidized bed: A hard-sphere approach," *Chem. Eng. Sci.* 51, 99 (1996).
- [22] B. H. Xu and A. B. Yu, "Numerical simulation of the gas-particle flow in a fluidized bed by combining discrete particle method with computational fluid dynamics," *Chem. Eng. Sci.* 52, 2785 (1997).
- [23] M. Ye, M. A. van der Hoef, and J. A. M. Kuipers, "A numerical study of fluidization behavior of Geldart A particles using a discrete particle simulation," *Powder Technol.* 139, 129 (2004).
- [24] J. N. Israelachvili, *Intermolecular and surface forces* (Academic Press, London, 1997).
- [25] J. P. K. Seville, C. D. W. Illett, and P. C. Knight, "Interparticle forces in fluidization: A review," *Powder Technol.* 113, 261 (2000).
- [26] C. Y. Wen and Y. H. Yu, "Mechanics of fluidization," *Chem. Eng. Prog. Ser.* 62, 100 (1966).
- [27] P. N. Rowe, "Drag forces in a hydraulic model of a fluidized bed: II," *Trans. Inst. Chem. Eng.* 39, 175 (1961).
- [28] M. Latzel, S. Luding, and H. J. Herrmann, "Macroscopic material properties from quasi-static, microscopic simulations of a two-dimensional shear-cell," *Gran. Matt.* 2, 123 (2000).
- [29] P. Duru, M. Nicolas, E. J. Hinch, and E. Guazzelli, "Constitutive laws of liquid-fluidized beds," *J. Fluid Mech.* 452, 371 (2002).
- [30] J. Li and J. A. M. Kuipers, "Gas-particle interactions in dense gas-fluidized beds," *Chem. Eng. Sci.* 58, 711 (2003).
- [31] J. Li and J. A. M. Kuipers, "On the origin of heterogeneous structure in dense gas(solid) flows," *Chem. Eng. Sci.* 60, 1251 (2005).
- [32] R. Jackson, "The mechanics of fluidized beds: I. The stability of the state of uniform fluidization," *Trans. Inst. Chem. Engrs.* 41, 13 (1963).
- [33] I. Goldhirsch and G. Zanetti, "Clustering instability in dissipative gases," *Phys. Rev. Lett.* 70, 1619 (1993).
- [34] N. Sela and I. Goldhirsch, "Hydrodynamic equations for rapid flows of smooth inelastic spheres, to Burnett order," *J. Fluid Mech.* 361, 41 (1998).
- [35] J. D. Erksen and S. Sundaresan, "A numerical study of planar wave instabilities in liquid-fluidized beds," *IUTAM Symposium on Computational Approaches to Multiphase Flow*, Proceedings of an IUTAM Symposium held at Argonne National Laboratory, October 4-7, 2004; Springer Series: Fluid Mechanics and its Applications, Vol. 81, Balachander, S, and Prosperetti, A. (eds.), Netherlands, (2006) pp 89-98.
- [36] D. C. Rapaport, *The Art of Molecular Dynamics Simulation*, (Cambridge University Press, Cambridge, 2004).
- [37] H. Rumpf, "The strength of granules and agglomerates," in *Agglomeration*, ed. W. A. Knepper (Interscience, New York, 1962).
- [38] J. F. Davidson, R. Clift, and D. Harrison (Editors), *Fluidization*, 2nd Ed. (Academic Press, London, 1985).
- [39] K. J. Dong, R. Y. Yang, R. P. Zou, and A. B. Yu, "Role of interparticle forces in the formation of random loose packing," *Phys. Rev. Lett.* 96, 145505 (2006).
- [40] C. H. Nam, R. Pfeifer, R. N. Dave, and S. Sundaresan, "Aerated vibro fluidization of Silica nanoparticles,"

- A IChE J. 50, 1776 (2004).
- [41] M. R. Mohan, R. N. Dave, and R. Pfeifer, "Promotion of deactivated sintering by dry-particle coating," A IChE J. 49, 604 (2004).
- [42] A. Mehta and G. C. Barker, "Vibrated powders: A microscopic approach," Phys. Rev. Lett. 67, 394 (1991).
- [43] J. J. McCarthy, T. Shinbrot, G. Metcalfe, D. E. Wolf, and J. M. Ottino, "Mixing of granular materials in slowly rotated containers," A IChE J. 42, 3351 (1996).
- [44] A. V. Potapov and C. S. Campbell, "Propagation of elastic waves in deep vertically shaken particle beds," Phys. Rev. Lett. 77, 4760 (1996).
- [45] P. W. Cleary, "Modelling comminution devices using DEM," Int. J. Numer. Anal. Meth. Geomech. 25, 83 (2001).
- [46] C. S. Campbell, "Granular shear flows at the elastic limit," J. Fluid Mech. 465, 261 (2002).
- [47] P. W. Cleary and M. L. Sawley, "DEM modelling of industrial granular flows: 3D case studies and the effect of particle shape on hopper discharge," Appl. Math. Modelling 26, 89 (2002).
- [48] J. W. Landry, G. S. Grest, L. E. Silbert, and S. J. Plimpton, "Coned granular packings: Structure, stress, and forces," Phys. Rev. E 67, 041303 (2003).
- [49] H. P. Zhu and A. B. Yu, "Steady-state granular flow in a three-dimensional cylindrical hopper with flat bottom: microscopic analysis," J. Phys. D: Appl. Phys. 37, 1497 (2004).
- [50] T. Kawaguchi, M. Sakamoto, T. Tanaka, and Y. Tsuji, "Quasi-three-dimensional numerical simulation of spouted beds in cylinder," Powder Technol. 109, 3 (2000).
- [51] S. McNamara and E. G. Flekkoy and K. J. Rognes Maloy, "Grains and gas flow: Molecular dynamics with hydrodynamic interactions," Phys. Rev. E 61, 4054 (2000).
- [52] M. J. Rhodes, X. S. Wang, M. Nguyen, P. Stewart, and K. Liman, "Onset of cohesive behaviour in gas fluidized beds: a numerical study using DEM simulation," Chem. Eng. Sci. 56, 4433 (2001).
- [53] H. Zhou, G. Flamant, and D. Gauthier, "DEM-LES of coal combustion in a bubbling fluidized bed. Part I: gas-particle turbulent flow structure," Chem. Eng. Sci. 59, 4193 (2004).
- [54] Y. Q. Feng, B. H. Xu, S. J. Zhang, A. B. Yu, and P. Zulli, "Discrete particle simulation of gas fluidization of particle mixtures," A IChE J. 50, 1713 (2004).
- [55] B. G. M. van Wachem, J. van der Schaaf, J. C. Schouten, R. Krishna, and C. M. van den Bleek, "Experimental validation of Lagrangian (Eulerian) simulations of fluidized beds," Powder Tech. 116, 155 (2001).
- [56] B. P. B. Hoopes, J. A. M. Kuipers, M. A. Mohd Salleh, M. Stein, and J. P. K. Seville, "Experimental validation of granular dynamics simulations of gas-fluidized beds with homogeneous inflow conditions using Positron Emission Particle Tracking," Powder Tech. 116, 166 (2001).
- [57] K. Anderson, S. Sundaresan, and R. Jackson, "Instabilities and the formation of bubbles in fluidized beds," J. Fluid Mech. 303, 327 (1995).
- [58] C. Guenther and M. Syam Lal, "The effect of numerical diffusion on isolated bubbles in a gas-solid fluidized bed," Powder Tech. 116, 142 (2001).
- [59] D. Geldart, "Types of gas fluidization," Powder Technol. 7, 285 (1973).
- [60] M. Alam and S. Luding, "First normal stress difference and crystallization in a dense sheared granular fluid," Phys. Fluid 15, 2298 (2003).
- [61] E. Apicella, M. D'Amore, G. Tardos, and R. Muri, "Onset of instability in sheared gas fluidized beds," A IChE J. 43, 1362 (1997).